Progress In Electromagnetics Research B, Vol. 93, 111–129, 2021

Mixed-Modulation Method for Adjusting Frequency and Voltage in the WPT Systems with Misalignments and Load Variations

Dingdou Wen[1], Yao Zou[1], Zhongqi Li[1, 2, *], and Jiliang Yi[1]

Abstract—The resonant frequency will be changed, and the load voltage will be unstable with misalignments and load variations in wireless power transfer (WPT) systems. In this paper, the expression for solving the resonant frequency is obtained. The calculation result shows that the resonant frequency is changed with the changes of misalignment and load. First, a new control method of frequency tracking with a Fuzzy proportional-integral (PI) compound controller is proposed, which can eliminate the overshoot of resonant frequency and improve the speed of frequency tracking. Second, a mixed-modulation method for adjusting frequency and voltage is further proposed, which is mainly composed of the selection algorithm of the duty cycle, the phase-shifting angle calculation, and the method of frequency tracking based on the Fuzzy PI compound controller. The appropriate duty cycle is obtained by the selection algorithm of the duty cycle to adjust the load voltage. The phase-shifting angles of different duty cycles are obtained by the phase-shifting angle calculation, which play a role in adjusting the resonant frequency by combining the Fuzzy PI compound controller. The proposed method can not only make the system keep a resonant state, but also make the output voltage across the load stable. A WPT system via magnetically coupled resonance is designed. Calculation and simulation results validating the superiority of the proposed method are given.

1. INTRODUCTION

Magnetically coupled resonance wireless power transfer (WPT) system has the advantages of safety, reliability, and flexible power supply. In recent years, WPT technology has become the focus of research [1–4] and has also been widely used in many applications, such as drones, medical devices, and aerospace [5–7]. The resonant frequency is an important parameter that affects the performance of a magnetically coupled resonance WPT system [8]. In practical application, the resonant frequency of a system is changed with the changes of misalignment and load, resulting in frequency detuning of the system. The frequency detuning will greatly reduce the transmission efficiency and output power of the system [9–11] and damage the reliability and safety of the system. Therefore, it is of great importance to study the method of frequency tracking in a WPT system. Now the available methods can be divided into the following three categories: the matching method, self-oscillating control method, and phase locking method.

The matching method is to match the resonant frequency of resonators to the operation frequency of the power source. This method is usually achieved by the impedance matching. An impedance-matching network was used to vary the resonant frequency of resonators at a certain distance to 13.56 MHz [12]. In order to improve the transfer power in cases that involved varying distances between resonators, the method that achieved adaptive matching by tuning the receiver circuit and matching network was introduced [13, 14]. However, it is difficult to achieve the matching of the input and output impedances,

---

Received 1 June 2021, Accepted 5 August 2021, Scheduled 16 August 2021

[*] Corresponding author: Zhongqi Li (my3eee@126.com).

[1] College of Electrical and Information Engineering, Hunan University of Technology, Zhuzhou 412007, China. [2] College of Electrical and Information Engineering, Hunan University, Changsha 410082, China.

which also increases the power loss of the system by the proposed method. An adaptive load matching network based on a capacitor matrix was further proposed [15]. The impedance values of load could be dynamically changed to maintain a reasonable level of maximum power transfer. However, this method focuses on impedance matching to improve the efficiency of the system. In addition, this method requires feedback across the load, and the response is very slow.

The self-oscillating control method with a multi-function integrated contactless transformer (MICT) was proposed [16], and a phase detection contactless current transformer was used for the transmission of the secondary current phase to the primary, where it was employed to drive the inverter switches. Reference [17] further considered the coupling relationship between the primary winding and the short-circuit current sensing winding, and a complete description of MICT was proposed to provide a more accurate analysis of the operation and control requirements. The results showed that the secondary current phase of the series/series compensation resonant converter was used to control the inverter. Better output controllability, dynamic response, and self-adaptability could be achieved simultaneously. However, the complex sensor design and shielding were required to eliminate electromagnetic interference and special compensation circuits, the phase delays are corrected in the sensing loop. In addition, a method of self-oscillating frequency tracking was proposed by tracking the damped natural frequency of the resonant circuit [18], and the frequency tracking was achieved within one half oscillation cycle. This proposed method was realized by synchronizing the working frequency with the damped natural frequency, which could eliminate the detuning effects caused by static and transient changes of the system. However, the control method of the self-oscillation frequency tracking is unstable, and there is always a slight tracking error between the damped natural frequency and the resonant frequency.

The phase locking method regulates the excitation frequency to maintain the zero phase angle (ZPA) between the loop voltage and the current at which the resonant state is achieved. This method is usually implemented by using a phase-locked loop (PLL). The frequency control from the primary side was proposed by tracking the ZPA of the input current and voltage with a PLL [19]. However, many variations such as relative position of coils or load changes cause a deviation of the resonant frequency, ultimately resulting in performance losses in the practical application. A self-adaptive tuning method with a PLL was proposed to improve the performance of systems at indefinite coil positions [20]. A dual looped self-adaptive control method was proposed, which was capable of tracking resonant frequency while maintaining a relatively stable induction voltage [21]. However, the induction voltage is sensitive to values of the coupling coefficient k, which is most relevant to the gap distance between coils, and cannot be compensated by using the proposed control loop. Therefore, misalignments are not studied in [21]. A method of frequency tracking with the PLL was proposed under the misalignment conditions [22]. The proposed method was achieved by continuously reducing the phase difference between the secondary current and the primary-side inverter output voltage. The method evaluated the PLL controller performance for the systems in continuous motion of variable velocity. It contributed to the evaluation of real-time frequency tracking controllers for rapidly moving systems. However, the duty cycle of the phase locking method with the PLL is generally fixed at 0.5, which makes the output voltage of the system fluctuate drastically with misalignments and load variations.

In this paper, a new control method of frequency tracking with a Fuzzy proportional-integral (PI) compound controller is proposed. Compared with the traditional PI controller, the compound controller can eliminate the overshoot of resonant frequency and improve the speed of frequency tracking. In addition, a mixed-modulation method for adjusting frequency and voltage is proposed. The duty cycle and frequency are simultaneously adjusted, which can maintain the voltage stability and resonant state of the system with misalignments and load variations. The superiority of the proposed method is proved by analyzing the MATLAB simulation results.

2. MATHEMATIC MODEL

The WPT system is composed of two resonant coils: transmitting and receiving resonant coils, labeled as Tx and Rx, as shown in Figure 1. d is the distance between Tx and Rx. Δ is the lateral misalignment between Tx and Rx. C_{Tx} is the external compensating capacitance of Tx, and C_{Rx} is the external compensating capacitance of Rx. The two-coil WPT system can be represented in terms of lumped circuit elements (L, C, and R) [23, 24]. As shown in Figure 2, parameter V_{s} is the source power, and

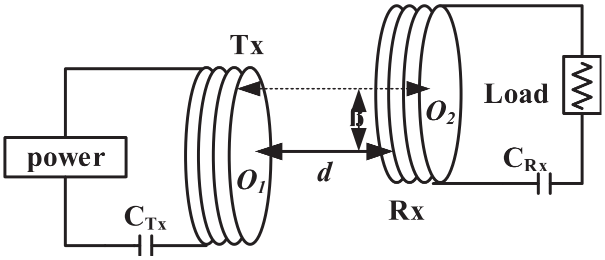

Figure 1. Simplified schematic of the WPT system based on magnetically coupling resonator.

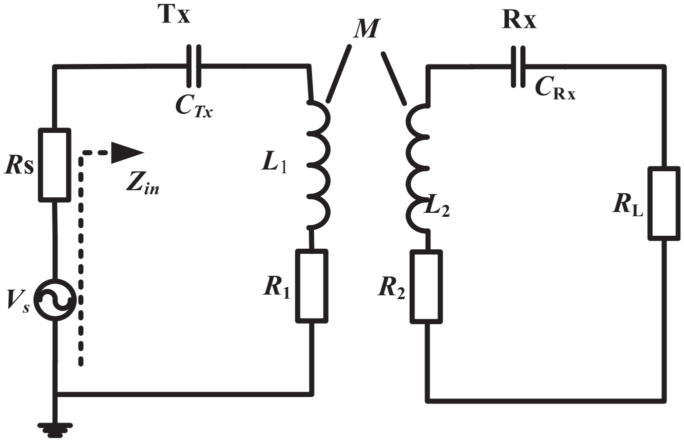

Figure 2. Equivalent circuit of the WPT system.

R_1 and R_2 are the parasitic resistors of Tx and Rx, respectively. R_s is the internal resistor of the power source, and R_L is the load resistor. L_1 and L_2 are the self-inductances of Tx and Rx. M is the mutual inductance between Tx and Rx. ω_0 is the original resonant angular frequency of each coil. ω is the operating angular frequency. ω_1 is the angular frequency of Tx ($\omega_1 = (L_1 C_\mathrm{Tx})^{-1/2}$), and ω_2 is the angular frequency of Rx ($\omega_2 = (L_2 C_\mathrm{Rx})^{-1/2}$). Z_{in} is the input impedance of the two-coil WPT system.

According to Kirchhoff's voltage law (KVL), the WPT system can be expressed as [25, 26]:

$$Z_1 \dot{I}_1 + j\omega M \dot{I}_2 = \dot{V}_s \tag{1}$$

$$j\omega M \dot{I}_1 + Z_2 \dot{I}_2 = 0 \tag{2}$$

$$Z_1 = R_s + R_1 + j\omega L_1 + 1/(j\omega C_{Tx}) \tag{3}$$

$$Z_2 = R_L + R_2 + j\omega L_2 + 1/(j\omega C_{Rx}) \tag{4}$$

where $\dot{I}_1$ is the current of Tx, and $\dot{I}_2$ is the current of Rx.

The expressions of $\dot{I}_1$ and $\dot{I}_2$ can be obtained by solving Eqs. (1) and (2).

$$\dot{I}_1 = \frac{Z_2 \dot{V}_s}{Z_1 Z_2 + (\omega M)^2} \tag{5}$$

$$\dot{I}_2 = -\frac{j\omega M \dot{V}_s}{Z_1 Z_2 + (\omega M)^2} \tag{6}$$

According to Eqs. (5) and (6), the expression of the efficiency is as follows:

$$\eta = \left| \frac{\dot{I}_2^2 R_\mathrm{L}}{\dot{V}_\mathrm{s} \dot{I}_1} \right| = \left| \frac{(\omega M)^2 R_L}{Z_1 {Z_2}^2 + (\omega M)^2 Z_2} \right| \tag{7}$$

Equations (3) and (4) are substituted into Eq. (7), and then the expression of efficiency can be obtained.

$$\eta = \left|\frac{\dot{I}_2^2\, R_{\mathrm{L}}}{\dot{V}_{\mathrm{s}}\, \dot{I}_1}\right| = \left|\frac{U^2 U_L}{\{(1+U_s+j\varepsilon_1 Q_1)(1+U_L+j\varepsilon_2 Q_2)^2 + (1+U_L+j\varepsilon_2 Q_2)U^2\}}\right| \tag{8}$$

The expression of the output power is as follows:

$$P_{out} = \left|\dot{I}_2^2\, R_L\right| = \left|\frac{U^2 U_L\, \dot{V}_s}{[(1+U_S+j\varepsilon_1 Q_1)\times(1+U_L+j\varepsilon_2 Q_2)+U^2]^2}\right| \tag{9}$$

where the source matching factor is defined as $U_s = R_s/R_1$, the load matching factor defined as $U_L = R_L/R_2$, the strong-coupling factor defined as $U = \omega_1 M/(R_1R_2)^{-1/2}$, the unload quality factor of Tx defined as $Q_1 = \omega L_1/R_1$, the unload quality factor of Rx defined as $Q_2 = \omega L_2/R_2$, the angular frequency deviation factor of Tx defined as $\varepsilon_1 = 1-\omega_1^2/\omega^2$, and the angular frequency deviation factor of Rx defined as $\varepsilon_2 = 1-\omega_2^2/\omega^2$.

By differentiating P_{out} with respect to ω and equating the differential function to zero.

$$\frac{\partial P_{out}}{\partial \omega} = 0 \tag{10}$$

According to Eq. (10), it is convenient to calculate the angular frequency corresponding to the maximum output power point with the help of MATLAB. The expression of the input impedance can be defined by Eq. (11).

$$Z_{in} = V_s/I_1 - R_s \tag{11}$$

According to Eqs. (3), (4), and (11), the expression of the input impedance can be obtained as follows:

$$Z_{in} = R_1 \frac{\begin{gathered}\{[(U^2+(1+U_s)(1+U_L)-Q_1Q_2\varepsilon_1\varepsilon_2)\\ +j(Q_1\varepsilon_1(1+U_L)+Q_2\varepsilon_2(1+U_s))][((1+U_L)-jQ_2\varepsilon_2)\}\end{gathered}}{(1+U_L)^2+Q_2^2\varepsilon_2^2} - R_s \tag{12}$$

Equation (12) can be simplified into Eq. (13).

$$Z_{in} = R_1 \frac{\left\{\left[(1+U_L)^2+U^2(1+U_L)+Q_2^2\varepsilon_2^2\right] + j\left[(1+U_L)^2 Q_1\varepsilon_1 + Q_1\varepsilon_1 Q_2^2\varepsilon_2^2 - U^2Q_2^2\varepsilon_2^2\right]\right\}}{(1+U_L)^2+Q_2^2\varepsilon_2^2} \tag{13}$$

According to Eq. (13), the input impedance characteristic angle (θ) between V_s and I_1 can be obtained as follows:

$$\theta = \arctan[\mathrm{Im}(Z_{in})/\mathrm{Re}(Z_{in}) \tag{14}$$

$$\theta = \arctan\left[\frac{(1+U_L)^2 Q_1\varepsilon_1 + Q_1Q_2^2\varepsilon_1\varepsilon_2^2 - U^2Q_2\varepsilon_2}{(1+U_L)^2+U^2(1+U_L)+Q_2^2\varepsilon_2^2}\right. \tag{15}$$

where $\mathrm{Re}(Z_{in})$ is the real component of Z_{in}. $\mathrm{Im}(Z_{in})$ is the imaginary component of Z_{in}. θ is the input impedance characteristic angle. When $\theta = 0$, the impedance is purely resistive, and Eq. (16) can be obtained from Eq. (15).

$$\begin{aligned}&\left(L_1L_2^2 - L_2M^2\right)\omega^6 + \left[(R_2+R_L)^2 L_1\right.\\ &- \left.2L_1L_2^2\omega_2^2 - L_1L_2^2\omega_1^2 + L_2M^2\omega_2^2\right]\omega^4\\ &+ [L_1L_2^2\omega_2^4 + 2L_1L_2^2\omega_1^2\omega_2^2 - (R_2+R_L)^2L_1\omega_1^2]\omega^2\\ &- L_1L_2^2\omega_1^2\omega_2^4 = 0\end{aligned} \tag{16}$$

The resonant angular frequencies of the WPT system can be obtained by solving Eq. (16). The resonant angular frequencies are dependent on M, C_{Tx}, C_1, C_{Rx}, L_2, R_L, R_1, and R_2. The parameters of each resonant coil are nearly constant. The resonant angular frequencies are mainly dependent on M and R_L, where M is changed with the changes of misalignment. Therefore, the resonant frequencies may be changed with the changes of misalignment and load. M is of great importance, which will be used to determine the coupling parameters between coils [27–29]. The most significant point is that the resonant frequency can be solved by Eq. (16) with the changes of each parameter of the coils.

3. FREQUENCY TRACKING METHOD WITH THE FUZZY PI COMPOUND CONTROLLER

In this section, a frequency tracking method with a Fuzzy PI compound controller is proposed. This compound controller is used to replace the traditional PI controller, which can eliminate the overshoot of resonant frequency and enhance the speed of frequency tracking. The control diagram of the proposed method is shown in Figure 3.

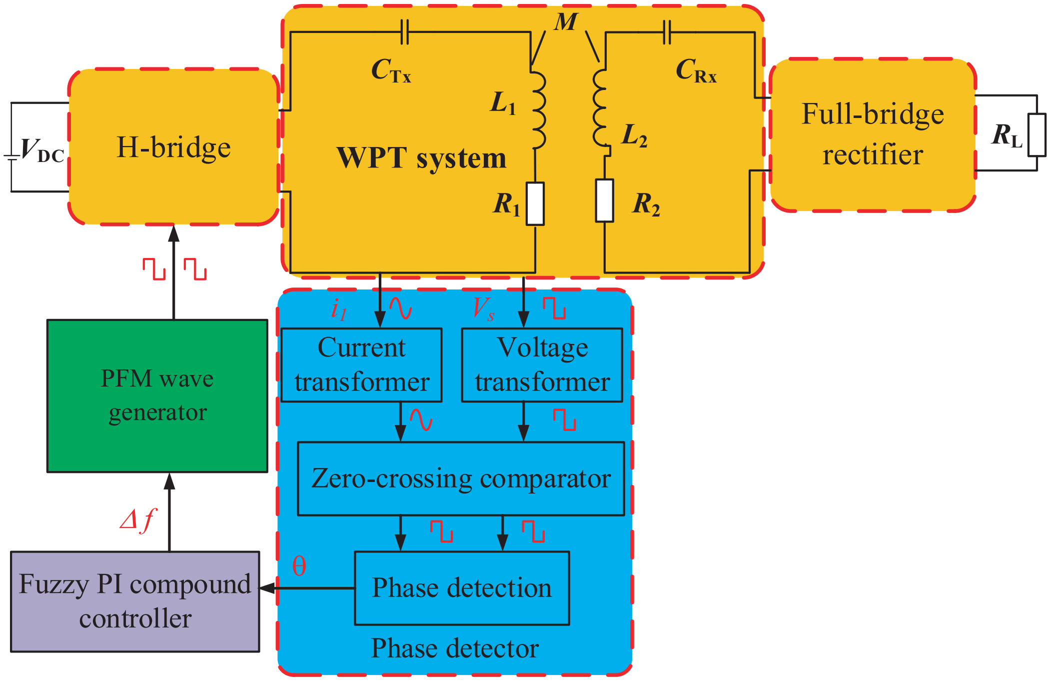

Figure 3. The diagram of method of frequency tracking.

This control method is mainly composed of a phase detector, a Fuzzy PI compound controller, and a pulse frequency modulation (PFM) waveform generator. The phase difference (θ) between the current signal (I_1) and voltage signal (V_s) is obtained by the phase detector. The control signal Δf is adjusted by the Fuzzy PI compound controller to reduce θ continuously. A square-wave driving signal of adjustable frequency is generated by the PFM waveform generator with Δf. The operating frequency is the resonant frequency when θ between V_s and I_1 is equal to zero. The implementation methods of each main part are described through the following sections.

3.1. Fuzzy PI Compound Controller

In this section, the Fuzzy PI compound controller can adjust the parameters of the PI controller by fuzzy rules, which can improve the speed of frequency tracking and reduce the overshoot of resonant frequency. Fuzzy control is a model-free method [30, 31], and this control can be directly obtained through induction and optimization according to the operator's theoretical research and operating experience. Strong anti-interference ability and robustness are the main advantages of fuzzy control. However, the fuzzy control has the disadvantages of low control accuracy and large static error. Therefore, a compound controller combining the advantages of both traditional PI and fuzzy control is proposed.

The control diagram of the Fuzzy PI compound controller is shown in Figure 4. The digital input signal is blurred through fuzzification. A fuzzy conclusion is obtained by fuzzy rules library. The precise quantity is obtained through defuzzification to achieve the control object and control goal. The phase deviation E and the rate of variation E_U are used as the digital input of the fuzzy controller. After

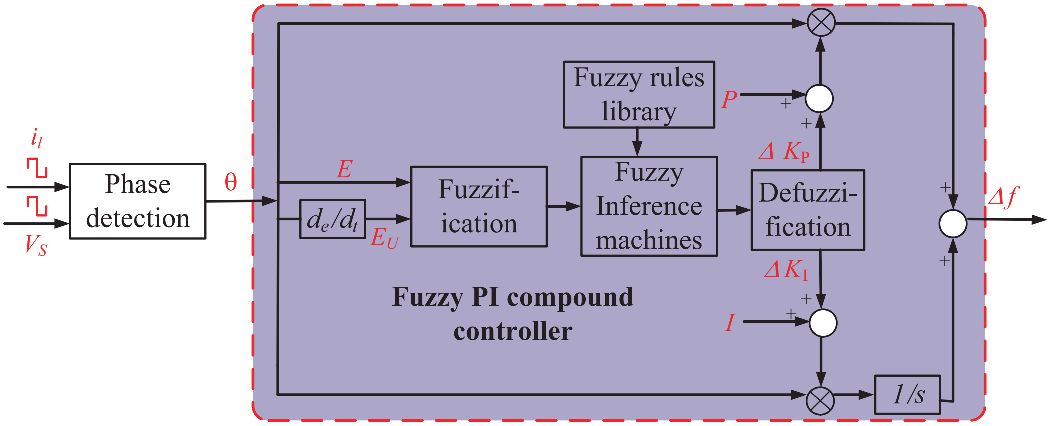

Figure 4. The control diagram of Fuzzy PI compound controller.

deblurring, two control variables ΔK_P and ΔK_I are considered as output.

$$\begin{cases} K_P = \Delta K_P + P \\ K_I = \Delta K_I + I \end{cases} \tag{17}$$

where P and I are the initial values of traditional PI controller and are obtained by conventional control methods. System parameters of P and I are optimized by controlling K_P and K_I of the compound controller in real time.

As shown in Figure 5, the fuzzy language and membership functions are established by considering the control effect and calculation amount. The fuzzy language is selected from seven commonly used symmetric linguistic variables: NB, NM, NS, ZO, PS, PM, PB, and the meaning is large negative, medium negative, small negative, zero, positive small, positive middle, positive big, respectively. The continuity domain is $[-6, 6]$. In order to facilitate the design of the controller and reduce the amount of calculation, the triangular function is selected for the membership function.

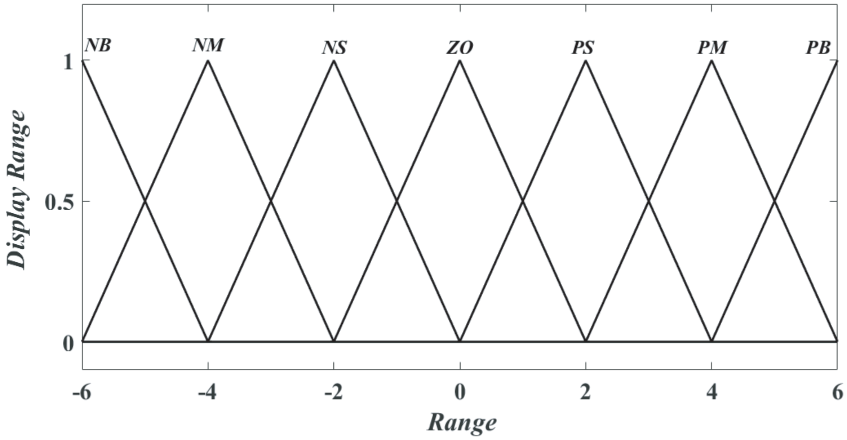

Figure 5. The graph of membership function.

The fuzzy rules are set by debugging experience of traditional control mode. The fuzzy controller contains 49 fuzzy rules. For the Fuzzy PI controller, the proportion coefficient and integral coefficient are independent of each other. Therefore, two fuzzy rules are established, as shown in Table 1 and Table 2. According to the fuzzy rules in Table 1 and Table 2, the spatial distribution of the input and output of the fuzzy controller can be obtained, as shown in Figure 6.

Table 1. Fuzzy rules of ΔK_P.

Eu	***E***						
	NB	**NM**	**NS**	**ZO**	**PS**	**PM**	**PB**
NB	PB	PB	PB	PB	PM	PS	ZO
NM	PB	PB	PB	PB	PM	ZO	ZO
NS	PM	PM	PM	PM	ZO	PS	PS
ZO	PM	PM	PS	ZO	NS	NM	PB
PS	PS	PS	ZO	NS	NM	NM	NM
PM	PS	ZO	NS	NM	NM	NM	NB
PB	ZO	ZO	NM	NM	NM	NB	NB

Table 2. Fuzzy rules of ΔK_I.

Eu	***E***						
	NB	**NM**	**NS**	**ZO**	**PS**	**PM**	**PB**
NB	NB	NB	NM	NM	NS	ZO	ZO
NM	NB	NB	NM	NS	NS	ZO	ZO
NS	NB	NM	NS	NS	ZO	PS	PS
ZO	NM	NM	NB	ZO	PM	NB	NB
PS	NM	NS	ZO	PS	PS	PM	PB
PM	ZO	ZO	PS	PS	PM	PB	PB
PB	ZO	ZO	PS	PM	PM	PB	PB

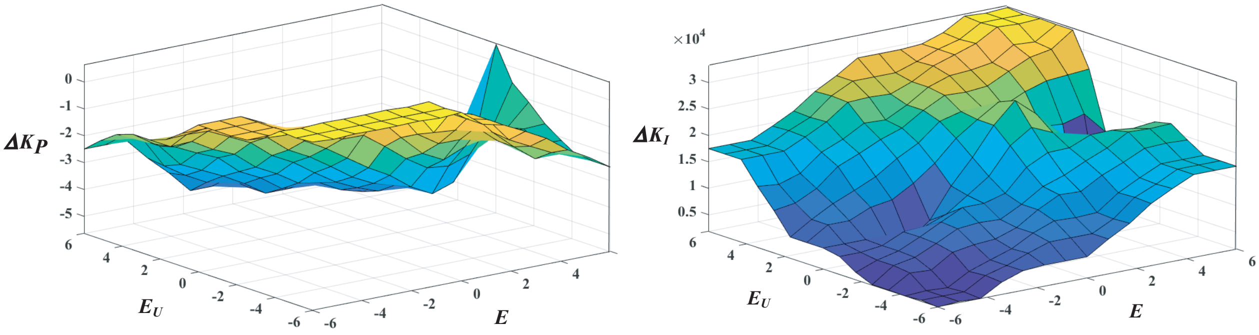

(a) (b)

Figure 6. The spatial distribution of the input and output of the fuzzy controller. (a) The spatial distribution of ΔK_P. (b) The spatial distribution of ΔK_I

As shown in Figure 4, the proportional coefficient P and integral coefficient I of the traditional PI controller keep unchanged; however, ΔK_P and ΔK_I of the output of fuzzy controller vary within a certain range. The frequency variable value (Δf) is more stable and accurate with the interaction of the coefficients.

3.2. Phase Detector

As shown in Figure 7, the phase detector is mainly composed of three stateflow modules. In this section, stateflow is used to achieve the function of phase detection. The rising edge signal of i_1 and V_s are captured, and the rising edge times t_1 and t_2 are output by stateflow 1 and stateflow 2, respectively. The period T can also be calculated by the functions of stateflow 1. The time difference between the rising edges of i_1 and V_s is calculated by stateflow 3. According to Eq. (18), the phase difference (θ) between i_1 and V_s can be obtained as follows:

$$\theta = \frac{t_1 - t_2}{T} * 360 \tag{18}$$

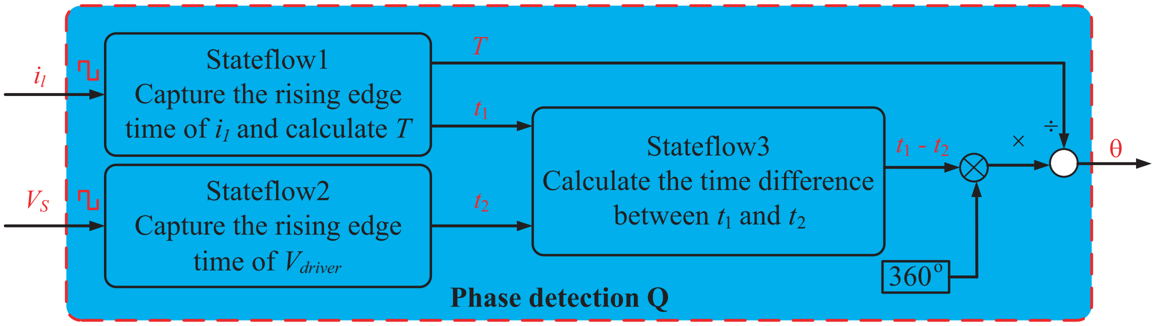

Figure 7. The control diagram of phase detector.

The interior structure of stateflows is shown in Figure 8. As shown in Figure 8(a), the pulse signal of the current i_1 is input and transferred to the state machine by default. The name of the state machine is obtain_rise_time, and the keyword of the state action is entry. It represents the execution of the corresponding action when the state action is activated. u is the input data of the system clock. Trigger event E1 has a self-loop transition and is executed once when every external event is triggered, where E1 is set as a rising edge trigger and is executed once when the corresponding rising edge is captured. The rising edge time of the input pulse i_1 can be continuously captured, and the time t_1 is output by the stateflow 1. The function of $n_1 = u$ is used to record and save the clock value of the current rising edge, and it is used as the period calculation data for the next state machine operation. T is obtained by subtracting n_1 from u. As shown in Figure 8(b), the pulse signal of V_s is input and transferred to the state machine by default. The rising edge time of the input pulse V_s can also be continuously captured, and the time t_2 is output by the stateflow 2. As shown in Figure 8(c), in order to use the rising edge signal of i_1 as the time point of phase calculation, the pulse signal of i_1 is input and transferred to the state machine by default, and then the rising edge time difference $(t_1 - t_2)$ of the square wave is obtained by the stateflow 3.

```
obtain_rise_time
entry:
t1=u,
T=u-n1,
n1=u;
```

(a)

```
obtain_rise_time
entry:
t2=u;
```

(b)

```
obtain_rise_time
entry:
y=t1-t2;
```

(c)

Figure 8. The interior structure of Stateflows. (a) Stateflow 1. (b) Stateflow 2. (c) Stateflow 3.

3.3. PFM Wave Generator

In this section, the PFM waveform generator is used to generate a square-wave driving signal, which is the driving signal of the adjustable frequency.

The frequency variable (Δf) is obtained by the Fuzzy PI compound controller, and the resonant frequency (f) is obtained by Δf plus the initial frequency (f_{int}). The counter is used to generate the sawtooth wave signal, and the counting form of the counter is the increment counting. The increment counting means that the counter increases from 0 to the period value T. When it reaches the period value, it starts the operation of the next cycle. Finally, as shown in Figure 9, a sawtooth wave is generated by the counter. The signal of the sawtooth wave is compared with the duty cycle of 0.5, and a square-wave signal of driving the H-bridge is generated.

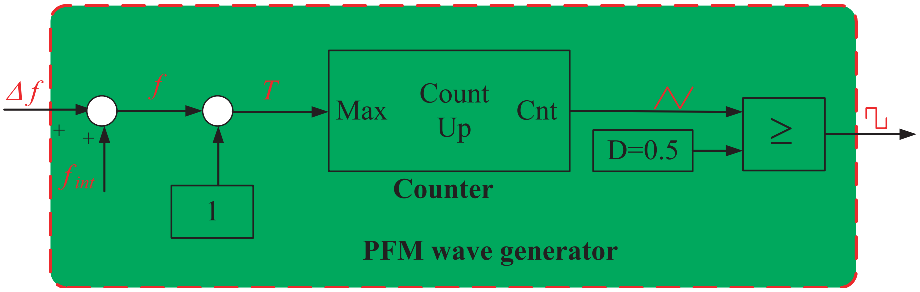

Figure 9. The diagram of the mixed-modulation method for adjusting frequency and voltage.

4. A MIXED-MODULATION METHOD FOR ADJUSTING FREQUENCY AND VOLTAGE

Under conditions of misalignment and load variation, the output voltage of the system is unstable when the duty cycle (D) is fixed at 0.5 with the traditional frequency tracking method. In this section, a mixed-modulation method for adjusting frequency and voltage is further proposed. The duty cycle and frequency are adjusted simultaneously by the proposed method, and it can maintain the voltage stability and resonant state of the system. The main mixed-modulation control method is shown in Figure 10.

This mixed-modulation method is mainly composed of the selection algorithm of the duty cycle, phase-shifting angle calculation, and method of frequency tracking based on the Fuzzy PI compound controller. D is fixed at 0.5 when the system does not work in a resonant state, and D varies from 0 to 0.5 when the system works in a resonant state by selection algorithm of the duty cycle. A square-wave signal is generated to drive the inverter when D is compared with the sawtooth wave signal. Finally, the function of voltage regulation has been achieved. The phase-shifting angle (θ_{Ref}) of different D is calculated by the phase-shifting angle calculation. The phase difference (θ') can be obtained by subtracting θ from θ_{Ref}. The Fuzzy PI compound controller is used to continuously adjust and reduce θ_{Ref}. Finally, the resonant frequency of the system is adjusted. The implementation methods of each main part are described through the following sections.

4.1. Phase-Shifting Angle Calculation

In this section, the phase-shifting angle calculation is obtained by the Fourier series expansion. Phase-shifting angles of different duty cycles are calculated by this expansion. It can keep a resonant state of the system by continuously adjusting the phase-shifting angle with the duty cycle variations. The

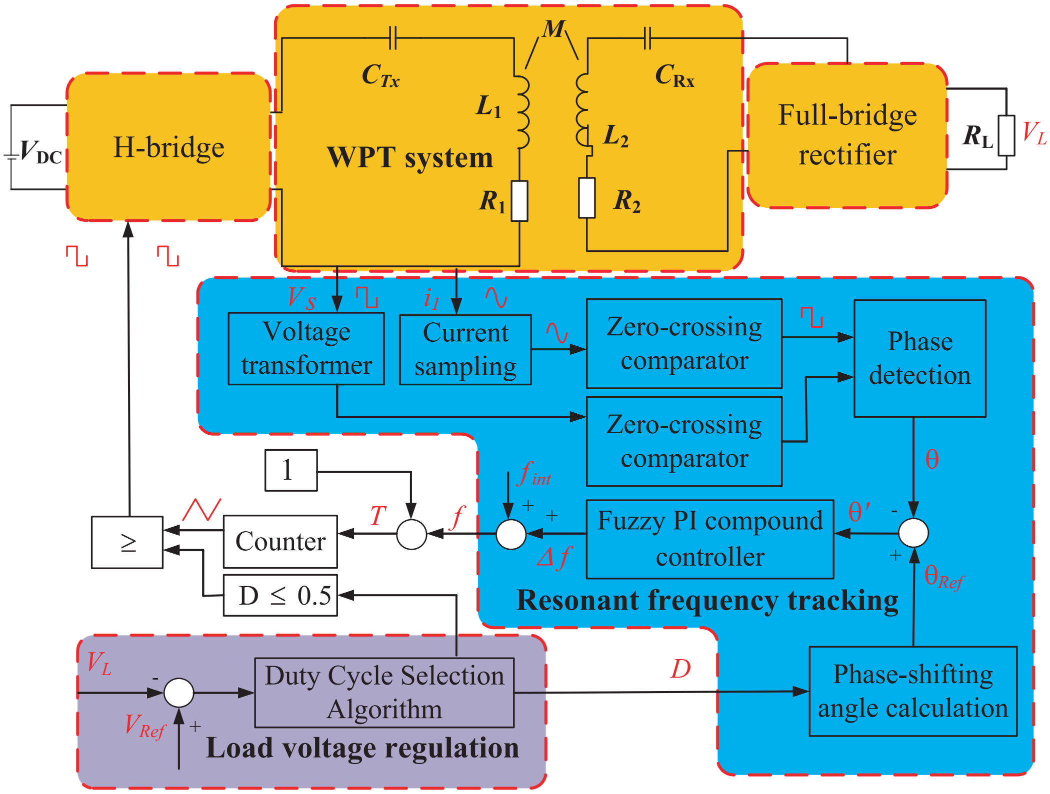

Figure 10. The diagram of PFM wave generator.

square-wave signal $V(t)$ can be defined by the Fourier series expansion:

$$V(t) = \frac{a_0}{2} + \sum_{n=1}^{\infty} [a_n \cos(n\omega_0 t) + b_n \sin(n\omega_0 t)] \tag{19}$$

$$a_0 = \frac{1}{T}\int_0^T V(t)dt \tag{20}$$

$$a_n = \frac{2}{T}\int_0^T V(t)\cos(n\omega_0 t)dt \tag{21}$$

$$b_n = \frac{2}{T}\int_0^T V(t)\sin(n\omega_0 t)dt \tag{22}$$

where a_0 is the direct current (DC) component, a_n the even function, and b_n the odd function.

(1) When D=0.5, the square wave signal $V(t)$ can be described as follows:

$$V(t) = \begin{cases} U & 0 < t < \frac{T}{2} \\ -U & \frac{T}{2} < t < T \end{cases} \tag{23}$$

where U is the amplitude variable of the square wave signal.

The expression of the DC component is obtained as follows:

$$a_0 = \frac{1}{T}\int_0^T V(t)\,dt = \frac{1}{T}\int_{-\frac{T}{2}}^{\frac{T}{2}} V(t)dt = 0 \tag{24}$$

According to Eqs. (21) and (22), the Fourier coefficients a_n and b_n are expressed as follows:

$$a_n = \frac{2}{T}\int_0^T V(t)\cos(n\omega_0 t)dt = \frac{2}{T}\int_{-\frac{T}{2}}^{\frac{T}{2}} V(t)\cos(n\omega_0 t)dt = 0 \tag{25}$$

$$\begin{aligned} b_n &= \frac{2}{T}\int_0^T V(t)\sin(n\omega_0 t)dt = \frac{2}{T}\int_{-\frac{T}{2}}^{0} -U\sin(n\omega_0 t)dt + \frac{2}{T}\int_{-\frac{T}{2}}^{0} U\sin(n\omega_0 t)dt \\ &= \frac{2U}{n\omega_0 T}\left[\cos(n\omega_0 t)\Bigg|_{-\frac{T}{2}}^{0} - \cos(n\omega_0 t)\Bigg|_{0}^{\frac{T}{2}}\right] = \frac{U}{\pi n}\left[2-2\cos(\pi n)\right] \end{aligned} \tag{26}$$

n can be divided into odd and even numbers, and b_n is decomposed as follows:

$$b_n = \begin{cases} \dfrac{4U}{\pi n} & n \text{ is odd} \\ 0 & n \text{ is even} \end{cases} \tag{27}$$

According to Eqs. (24), (25), and (27), the Fourier series expansion of the signal is as follows:

$$V(t) = \frac{4U}{\pi}\left(\sin\omega_0 + \frac{1}{3}\sin(3\omega_0 \mathrm{t}) + \frac{1}{5}\sin(5\omega_0 \mathrm{t}) + \ldots \frac{1}{n}\sin(n\omega_0 \mathrm{t})\right) \tag{28}$$

It can be found that the expression only contains the first, third, fifth, and nth odd harmonics. In the section, only the fundamental component is considered. θ_{Ref} is equal to 0° with $D = 0.5$.

(2) When $D = 0.4$, the freewheeling of the square wave signal needs to be considered, and the square wave signal $V(t)$ can be expressed by Eq. (29).

$$V(t) = \begin{cases} U & t \in (0, 0.4T) \cup (0.45T, 0.5T) \cup (0.9T, 0.95T) \\ -U & t \in (0.4T, 0.45T) \cup (0.5T, 0.9T) \cup (0.95T, T) \end{cases} \tag{29}$$

The expression of the DC component is as follows:

$$a_0 = \frac{1}{T}\int_0^T V(t)dt = \frac{1}{T}\left(\begin{aligned} &\int_0^{0.4T} Udt + \int_{0.45T}^{0.5T} Udt + \int_{0.9T}^{0.95T} Udt \\ &- \int_{0.4T}^{0.45T} Udt - \int_{0.5T}^{0.9T} Udt - \int_{0.95T}^{T} Udt \end{aligned}\right) = 0 \tag{30}$$

The Fourier coefficients a_n and b_n can be obtained as follows:

$$\begin{aligned} a_n &= \frac{2}{T}\int_0^T V(t)\cos(n\omega_0 t)dt = \frac{2}{T}\left[\begin{aligned} &\int_0^{0.4T} U\cos(n\omega_0 t)dt + \int_{0.45T}^{0.5T} U\cos(n\omega_0 t)dt \\ &+ \int_{0.9T}^{0.95T} U\cos(n\omega_0 t)dt - \int_{0.4T}^{0.45T} U\cos(n\omega_0 t)dt \\ &- \int_{0.5T}^{0.9T} U\cos(n\omega_0 t)dt - \int_{0.95T}^{T} U\cos(n\omega_0 t)dt \end{aligned}\right] \\ &= \frac{2U}{\pi n}\left(\sin 0.8\pi n + \sin 1.9\pi n - \sin 0.9\pi n - \sin 1.8\pi n\right) \end{aligned} \tag{31}$$

$$b_n = \frac{2}{T}\int_0^T V\left(t\right)\sin\left(n\omega_0 t\right)dt$$

$$= \frac{2}{T}\left[\begin{array}{l} \int_{0}^{0.4T} U\sin\left(n\omega_0 t\right)dt + \int_{0.45T}^{0.5T} U\sin(n\omega_0 t)dt \\ + \int_{0.9T}^{0.95T} U\sin\left(n\omega_0 t\right)dt - \int_{0.4T}^{0.45T} U\sin\left(n\omega_0 t\right)dt \\ - \int_{0.5T}^{0.9T} U\sin\left(n\omega_0 t\right)dt - \int_{0.95T}^{T} U\sin\left(n\omega_0 t\right)dt \end{array}\right]$$

$$= \frac{2U}{\pi n}\left(\begin{array}{l} -\cos 0.8\pi n - \cos 1.9\pi n \\ +\cos 0.9\pi n + 1 - \cos\pi n \end{array}\right) \tag{32}$$

n can be divided into odd and even numbers as follows:

$$b_n = \begin{cases} \frac{2U}{\pi n}\left(\begin{array}{l} -\cos 0.8\pi n - \cos 1.9\pi n \\ +\cos 0.9\pi n + \cos 1.8\pi n + 2 \end{array}\right) & n \text{ is odd} \\ \frac{2U}{\pi n}\left(\begin{array}{l} -\cos 0.8\pi n - \cos 1.9\pi n \\ +\cos 0.9\pi n + \cos 1.8\pi n \end{array}\right) & n \text{ is even} \end{cases} \tag{33}$$

When n is the even number, $V(t)$ is equal to zero with the help of MATLAB. When n is the odd number, according to Eqs. (30), (31), and (33) the square wave signal $V(t)$ is as follows:

$$V(t) = \frac{2U}{\pi}\left[\begin{array}{l} 1.8\sin\left(\omega_0 t + \frac{\pi}{10}\right) + \frac{0.35}{3} \times \sin\left(3\omega_0 t + \frac{3\pi}{10}\right) \\ +\frac{2}{5} \times \sin\left(5\omega_0 t - \frac{\pi}{2}\right) + \frac{4.35}{7} \times \sin\left(7\omega_0 t - \frac{3\pi}{10}\right) + \ldots \end{array}\right] \tag{34}$$

In this section, only the fundamental component is considered, and θ_{Ref} is equal to $\pi/10$ with $D = 0.4$. Similarly, the calculation result of other duty cycles can be obtained by the Fourier series expansion.

In summary, the calculation in Eqs. (19)–(34) of the phase-shifting angle with different duty cycles can be simplified to Eq. (35) by the induction and summary method. According to Eq. (35), $\theta_{Ref} = 0°$ when $D = 0.5$, and $\theta_{Ref} = \pi/10$ when $D = 0.4$. Other different duty cycles can also be calculated by Eq. (35). The results of Eq. (35) are consistent with the results of the Fourier series expansion.

$$\theta_{Ref} = \frac{0.5T - DT}{2} \times 360° \times \frac{1}{T} \tag{35}$$

where D is the duty cycle of the pulse of driving the inverter switch, T the period, and θ_{Ref} the phase-shifting angle of different duty cycles.

4.2. Selection Algorithm of the Duty Cycle

In this section, the selection algorithm of the duty cycle is proposed to output the appropriate duty cycle with different resonant frequencies.

The difference between the initial voltage (V_{Ref}) and load voltage (V_L) is input into the selection algorithm. A flowchart of the selection algorithm of the duty cycle is shown in Figure 11. Step 1: D is fixed at 0.5, and the resonant frequency (f) is adjusted by frequency tracking method with the Fuzzy PI compound controller. Step 2: If f can be searched, then the program proceeds to the third step, whereas the program returns to the first step. Step 3: Starting to adjust $D < 0.5$ by PI controller, and then D is output, and V_L can also be stable with different misalignments and load variations.

5. SIMULATION RESULT AND ANALYSIS

5.1. Simulation Verification of the Frequency Calculation

In this section, the resonant frequencies at the maximum efficiency point and the frequencies at the maximum output power point are calculated by using Eq. (16) and Eq. (10), respectively. The

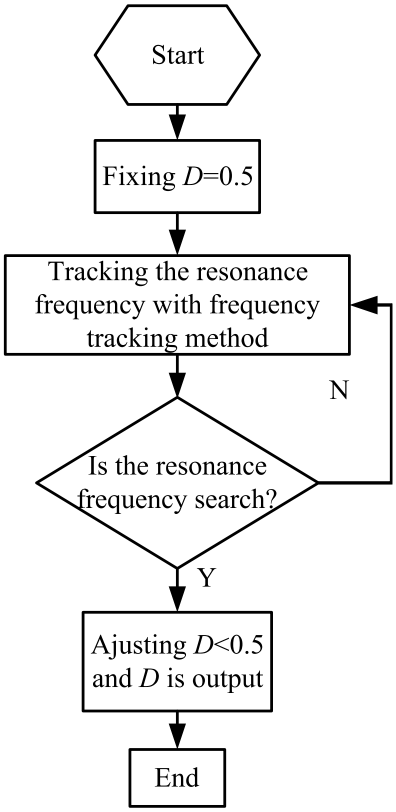

Figure 11. Flowchart of selection algorithm of the different duty cycle.

correctness of Eq. (16) and Eq. (10) is verified by simulation operation with the help of MATLAB. It is found that the system may have multiple resonant frequencies, and the frequency at the maximum efficiency point is very close to that of the maximum output power point. The system may work at the maximum efficiency point and maximum output power point simultaneously by adjusting the operating frequency. The parameters of each coil are shown in Table 3.

Table 3. Detailed parameters of each coil.

Symbol	Value
$L_1/\mu\text{H}$	353.680
$L_2/\mu\text{H}$	216.020
C_1/nF	9.860
C_2/nF	16.090
R_1/Ω	0.438
R_2/Ω	0.281
f_0/kHz	85.000
R_L/Ω	10.000

Figure 12(a) shows the input impedance characteristic angle versus the operating angular frequency with different misalignments. When the input impedance characteristic angle is equal to zero, the angular frequency is the resonant angular frequency. It can be clearly seen that there may be three resonant frequencies in the WPT system. Figure 12(b) shows the relationship between efficiency and

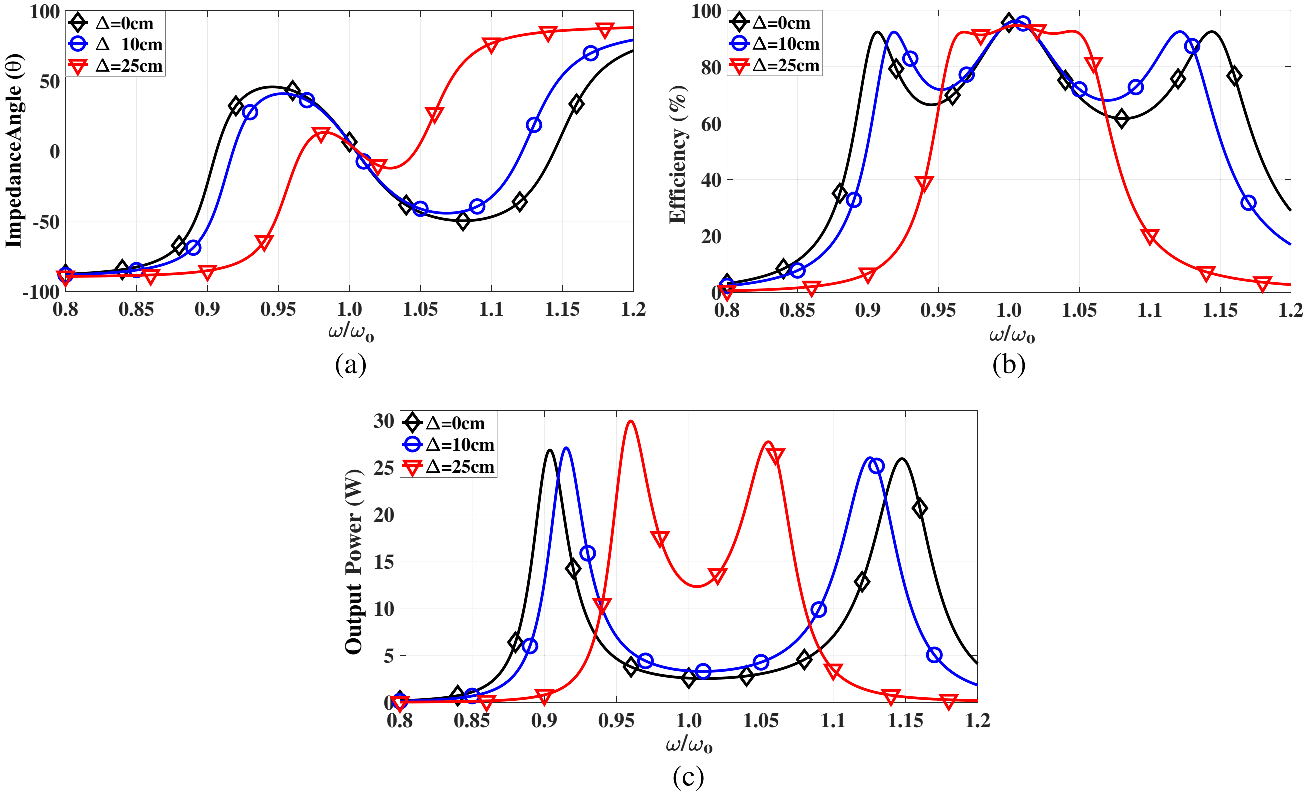

Figure 12. Input impedance characteristic angle, efficiency, and output power versus ω/ω_0 with different misalignments. (a) Input impedance characteristic angle versus ω/ω_0. (b) Efficiency versus ω/ω_0. (c) Output power versus ω/ω_0.

operating angular frequency. The results show that the efficiency is higher at the resonant frequency. Figure 12(c) shows the relationship between output power and operating angular frequency. It is found that there are two maximum output power points in the WPT system.

In summary, it is found that the output power at the original resonant frequency (85 kHz) is at very low point, and the efficiency at 85 kHz is at the maximum point; however the output power and the efficiency at the left and right sides of 85 kHz are both at the maximum point. If the system works at the maximum efficiency point and the maximum output power point simultaneously, it can directly track the resonant frequency of the left and right sides of the original resonant frequency (85 kHz).

5.2. Simulation Verification of Frequency Tracking Method

In order to evaluate the proposed method with different misalignments and load variations, the method of frequency tracking based on the traditional PI controller and the Fuzzy PI compound controller are studied, respectively. Figure 13 shows the frequency during start-up with different controllers and different misalignments. The simulation results show that the Fuzzy PI compound controller has the advantages of no overshoot of the resonant frequency and high speed of the frequency tracking.

As shown in Figure 13(a), during start-up, the frequency tracking of the traditional PI controller shows overshoot and takes 0.0075 seconds to reach the steady state, while the frequency tracking of the Fuzzy PI compound controller has no overshoot, and takes only 0.005 seconds to reach the steady state. The steady state represents that the system has work in the resonant state, and the resonant frequency is 76.93 kHz. At 0.015 seconds, the misalignment (Δ) between Tx and Rx suddenly varies from 0 cm to 10 cm. The resonant frequency rises from 76.93 kHz to 77.96 kHz. The Fuzzy PI compound controller has advantage with no overshoot of the resonant frequency. As shown in Figure 13(b), during start-up, the frequency tracking of the traditional PI controller rises sharply, exhibits great overshoot, and takes

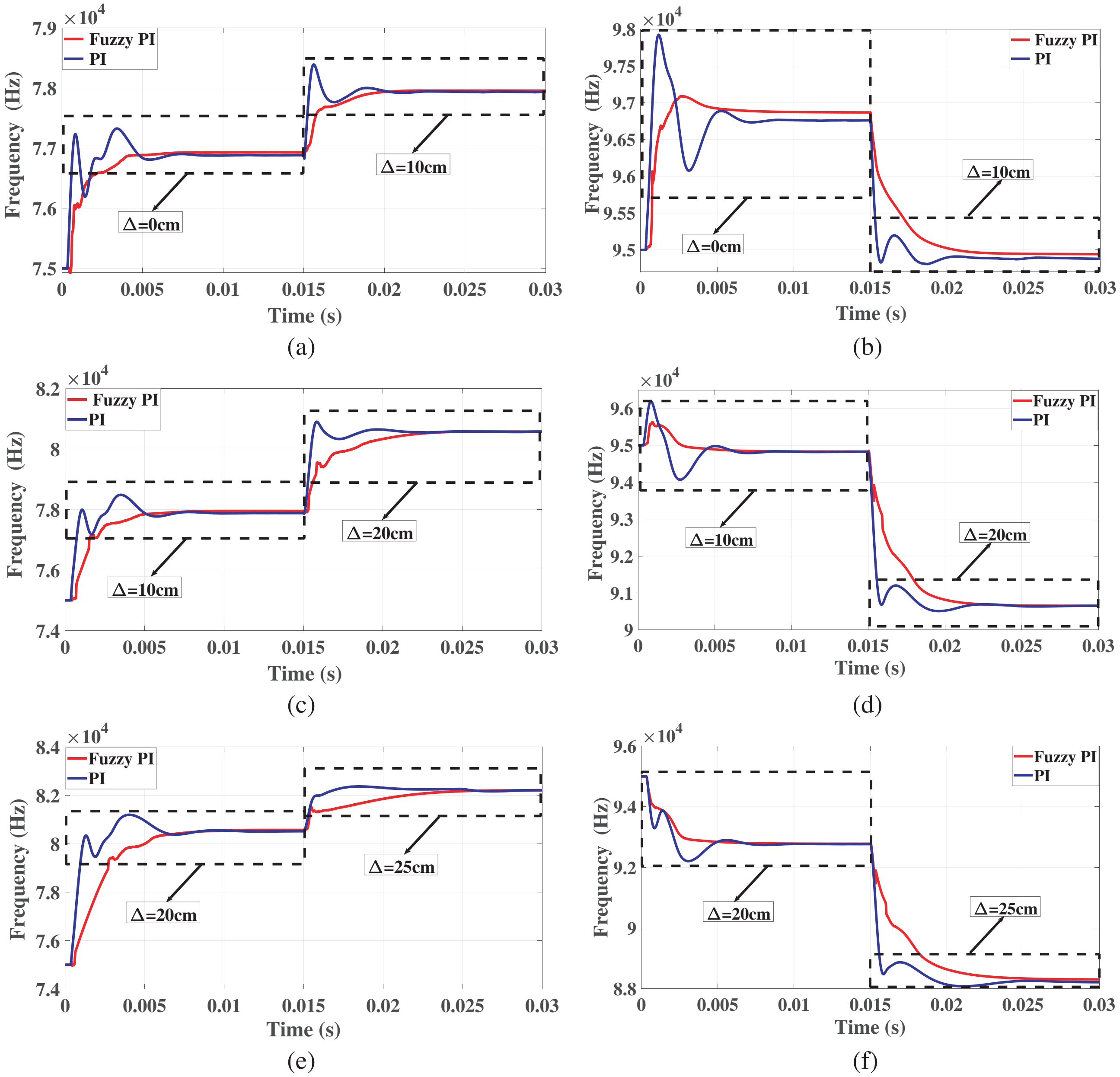

(a) (b) (c) (d) (e) (f)

Figure 13. Frequency of the traditional PI and the Fuzzy PI compound controllers with different misalignments. (a) Frequency of the left side of 85 kHz with Δ varied from 0 cm to 10 cm. (b) Frequency of the right side of 85 kHz with Δ varied from 0 cm to 10 cm. (c) Frequency of the left side of 85 kHz with Δ varied from 10 cm to 20 cm. (d) Frequency of the right side of 85 kHz with Δ varied from 10 cm to 20 cm. (e) Frequency of the left side of 85 kHz with Δ varied from 20 cm to 25 cm. (f) Frequency of the right side of 85 kHz with Δ varied from 20 cm to 25 cm.

a long time to reach the steady state, while the frequency tracking of the Fuzzy PI compound controller shows less overshoot and quickly reaches the steady state. The resonant frequency is 96.87 kHz. At 0.015 seconds, Δ between Tx and Rx suddenly also varies from 0 cm to 10 cm. The resonant frequency drops from 96.87 kHz to 94.94 kHz. As shown in Figure 13(c), during start-up, the frequency tracking of the traditional PI controller shows great overshoot and takes 0.0075 seconds to reach the steady state, while the frequency tracking of the Fuzzy PI compound controller has no overshoot and takes only 0.005 seconds to reach the steady state. The resonant frequency is 77.96 kHz. At 0.015 seconds,

Δ suddenly varies from 10 cm to 20 cm. The resonant frequency rises from 77.96 kHz to 80.58 kHz. As shown in Figure 13(d), during start-up, the frequency tracking of the traditional PI controller rises sharply and exhibits great overshoot, while the frequency tracking of the Fuzzy PI compound controller shows less overshoot. The resonant frequency is 94.94 kHz. At 0.015 seconds, Δ between Tx and Rx suddenly also varies from 10 cm to 20 cm. The resonant frequency drops from 94.94 kHz to 90.61 kHz. As shown in Figure 13(e), during start-up, the frequency tracking of the traditional PI controller shows great overshoot, while the frequency tracking of the Fuzzy PI compound controller has no overshoot, and the resonant frequency is 80.58 kHz. At 0.015 seconds, Δ suddenly varies from 20 cm to 25 cm. The resonant frequency rises from 80.58 kHz to 82.28 kHz. As shown in Figure 13(f), during start-up, the frequency tracking of the traditional PI controller takes 0.007 seconds to reach the steady state, while the frequency tracking of the Fuzzy PI compound controller takes only 0.005 seconds to reach the steady state. The resonant frequency is 90.61 kHz. At 0.015 seconds, Δ between Tx and Rx suddenly also varies from 20 cm to 25 cm. The resonant frequency drops from 90.61 kHz to 82.28 kHz.

In summary, the method of the frequency tracking of the Fuzzy PI compound controller is better than that of the traditional PI controller.

5.3. Simulation Verification of the Mixed-Modulation Method

Figure 14 shows the output voltage (V_L) versus time with the frequency tracking method. The results show that V_L across the load (R_L) is unstable with different misalignments and different loads.

Figure 15 shows the result of V_L versus time with the mixed-modulation method. The simulation results show that the output voltage can be stable with different misalignments and different loads. The value of output voltage (V_{Ref}) is adjusted by simulation, and finally V_{Ref} is set at 12 V. As shown in

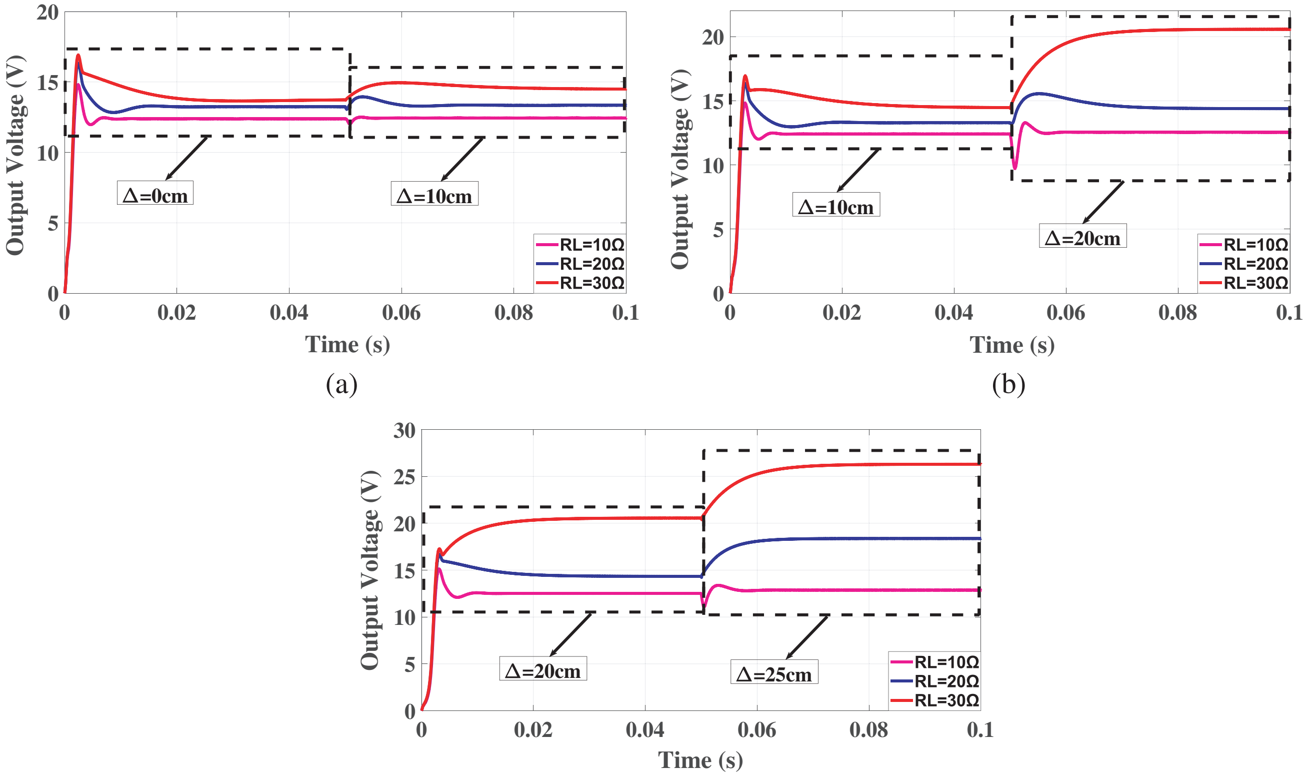

(a)

(b)

(c)

Figure 14. Output voltage versus time with the frequency tracking method. (a) The output voltage with Δ varied from 0 cm to 10 cm. (b) The output voltage with Δ varied from 10 cm to 20 cm. (c) The output voltage with Δ varied from 20 cm to 25 cm.

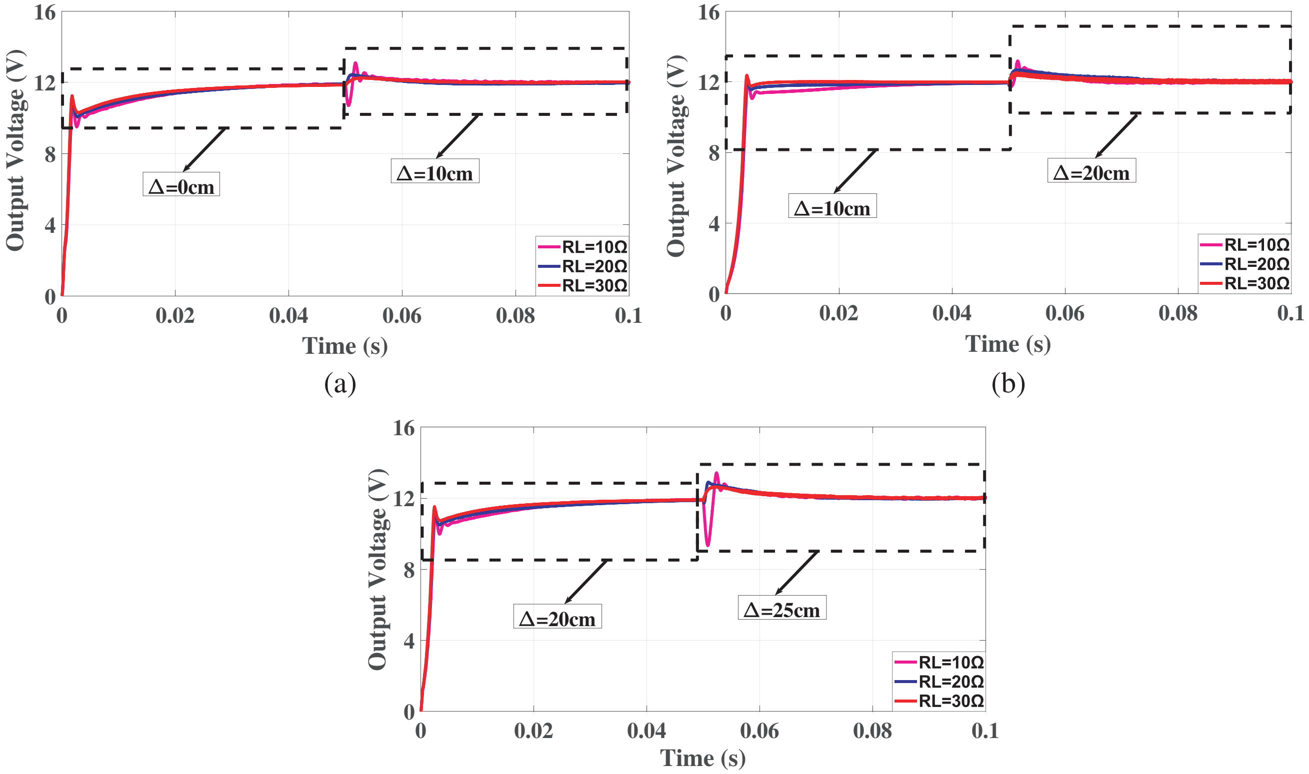

(a) (b)

(c)

Figure 15. Output voltage versus time with the mixed-modulation method of adjusting frequency and voltage. (a) The output voltage with Δ varied from 0 cm to 10 cm. (b) The output voltage with Δ varied from 10 cm to 20 cm. (c) The output voltage with Δ varied from 20 cm to 25 cm.

Figure 15(a), in the time period of 0–0.05 seconds, V_L can be stabilized at around 12 V by the proposed method with $R_L = 10\,\Omega$, $20\,\Omega$, and $30\,\Omega$. At 0.05 seconds, Δ between Tx and Rx suddenly varies from 0 cm to 10 cm. V_L is still stabilized at around 12 V by the mixed-modulation method at 0.06 seconds. As shown in Figure 15(b), in the time period of 0–0.05 seconds, V_L can also be stabilized at around 12 V by the proposed method with $R_L = 10\,\Omega$, $20\,\Omega$, and $30\,\Omega$. At 0.05 seconds, Δ between Tx and Rx suddenly varies from 10 cm to 20 cm. V_L is still stabilized at around 12 V by the mixed-modulation method at 0.065 seconds. As shown in Figure 15(c), in the time period of 0–0.05 seconds, V_L can also be stabilized at around 12 V by the proposed method with $R_L = 10\,\Omega$, $20\,\Omega$, and $30\,\Omega$. At 0.05 seconds, Δ between Tx and Rx suddenly varies from 20 cm to 25 cm. V_L is still stabilized at around 12 V by the mixed-modulation method at 0.07 seconds.

In summary, the simulation results show that the output voltage across the load can be stable with misalignments and load variations by the mixed-modulation method in Figure 15.

6. CONCLUSION

In this paper, a control method of frequency tracking based on the Fuzzy PI compound controller is proposed with misalignments and load variations. Compared with the traditional PI controller, the proposed method can further reduce the overshoot of resonant frequency and improve the stability of frequency tracking. In addition, a mixed-modulation method for adjusting frequency and voltage is further proposed. The duty cycle and frequency are adjusted simultaneously by the proposed method, and it can not only make the system reach a resonant state, but also make the output voltage stable. Simulation results and comparative studies validate the superiority of two methods with misalignments and load variations.

In the future, the full duty cycle of the method of the frequency tracking will be studied. The Z source will be added to the inverter, which can solve the problem caused by the direct connection of the inverter when $D > 0.5$.

ACKNOWLEDGMENT

This work was supported in part by the National Natural Science Foundation of China under Grant 11901188, in part by the Natural Science Foundation of Hunan Province under Grants 2018JJ3127 and 2019JJ60055, in part by the Outstanding Youth Project of Hunan Education Department under Grants 20B186 and 18A272.

REFERENCES

1. Cheng, C. and F. Lu, "Load-independent wireless power transfer system for multiple loads over a long distance," *IEEE Transactions on Power Electronics*, Vol. 34, No. 9, 9279–9288, Sept. 2019.
2. Correia, R. and N. B. Carvalho, "Ultrafast backscatter modulator with low-power consumption and wireless power transmission capabilities," *IEEE Microwave and Wireless Components Letters*, Vol. 27, No. 12, 1152–1154, Dec. 2017.
3. Zhang, Y. and T. Lu, "Selective wireless power transfer to multiple loads using receivers of different resonant frequencies," *IEEE Transactions on Power Electronics*, Vol. 30, No. 11, 6001–6005, Nov. 2015.
4. Jin, K. and W. Zhou, "Wireless laser power transmission: A review of recent progress," *Transactions on Power Electronics*, Vol. 34, No. 4, 3842–3859, Apr. 2019.
5. Wang, Z. and W. Xu, "Joint trajectory optimization and user scheduling for rotary-wing UAV-enabled wireless powered communication networks," *IEEE Access*, Vol. 7, 181369–181380, Dec. 2019.
6. Liu, C. and C. Jiang, "An effective sandwiched wireless power transfer system for charging implantable cardiac pacemaker," *IEEE Transactions on Industrial Electronics*, Vol. 66, No. 5, 4108–4117, May 2019.
7. Yoshida, S. and N. Hasegawa, "Experimental demonstration of microwave power transmission and wireless communication within a prototype reusable spacecraft," *IEEE Microwave and Wireless Components Letters*, Vol. 25, No. 8, 556–558, Aug. 2015.
8. Mastri, F. and A. Costanzo, "Coupling-independent wireless power transfer," *IEEE Microwave and Wireless Components Letters*, Vol. 26, No. 3, 222–224, Mar. 2016.
9. Najjarzadegan, M. and I. Ghotbi, "Improved wireless power transfer efficiency using reactively terminated resonators," *IEEE Antennas and Wireless Propagation Letters*, Vol. 17, No. 5, 803–807, May 2018.
10. Hui, S. Y. R. and W. Zhong, "A critical review of recent progress in mid-range wireless power transfer," *IEEE Transactions on Power Electronics*, Vol. 29, No. 9, 4500–4511, Sept. 2014.
11. Lim, Y. and H. Tang, "An adaptive impedance-matching network based on a novel capacitor matrix for wireless power transfer," *IEEE Transactions on Power Electronics*, Vol. 29, No. 8, 4403–4413, Aug. 2014.
12. Teck, C. B. and I. Takehiko, "Basic study of improving efficiency of wireless power transfer via magnetic resonance coupling based on impedance matching," *IEEE International Symposium on Industrial Electronics*, 2011–2016, Nov. 2010.
13. Trevor, S. B. and R. Nicholas, "Antenna impedance matching for maximum power transfer in wireless sensor networks," *IEEE Sensors*, 916–919, Oct. 2009.
14. Kim, N. Y. and K. Y. Kim, "Adaptive frequency with power-level tracking system for efficient magnetic resonance wireless power transfer," *Electronics Letters*, Vol. 48, No. 8, 452, Mar. 2012.
15. Lim, Y. and H. Tang, "An adaptive impedance-matching network based on a novel capacitor matrix for wireless power transfer," *IEEE Transactions on Power Electronics*, Vol. 29, No. 8, 4403–4413, Aug. 2014.

16. Xu, L. and Q. Chen, "Self-oscillating contactless resonant converter with power transfer and current sensing integrated transformer," *IEEE Energy Conversion Congress and Exposition (ECCE)*, 4539–4543, Sept. 2015.
17. Xu, L. and Q. Chen, "Self-oscillating resonant converter with contactless power transfer and integrated current sensing transformer," *IEEE Transactions on Power Electronics*, Vol. 32, No. 6, 4839–4851, Jun. 2017.
18. Xie, K. and A. Huang, "Half-cycle resonance tracking for inductively coupled wireless power transmission system," *IEEE Transactions on Power Electronics*, Vol. 33, No. 3, 2668–2679, Mar. 2018.
19. Fu, B. Z. W. and D. Qiu, "Study on frequency-tracking wireless power transfer system by resonant coupling," *IEEE 6th Int. Power Electronics and Motion Control Conference*, 2658–2663, May 2009.
20. Wang, J. and Z. Zhu, "PLL-based self-adaptive resonance tuning for a wireless-powered potentiometer," *IEEE Transactions on Circuits and Systems II: Express Briefs*, Vol. 60, No. 7, 392–396, Jul. 2013.
21. Xie, K. and A. F. Huang, "Modular high-voltage bias generator powered by dual-looped self-adaptive wireless power transmission," *Rev. Sci. Instrum.*, Vol. 86, No. 4, 044707, Apr. 2015.
22. Gati, E. and G. Kampitsis, "Variable frequency controller for inductive power transfer in dynamic conditions," *IEEE Transactions on Power Electronics*, Vol. 32, No. 2, 1684–1696, Feb. 2017.
23. Lu, F. and H. Zhang, "A dual-coupled LCC-compensated IPT system to improve misalignment performance," *IEEE PELS Workshop on Emerging Technologies: Wireless Power Transfer (WoW)*, 1–8, May 2017.
24. Yang, J. and X. Zhang, "An LCC-SP compensated inductive power transfer system and design considerations for enhancing misalignment tolerance," *IEEE Access*, 1, Oct. 2020.
25. Lee, C. K. and W. X. Zhong, "Effects of magnetic coupling of nonadjacent resonators on wireless power domino-resonator systems," *IEEE Transactions on Power Electronics*, Vol. 27, No. 4, 1905–1916, Apr. 2012.
26. Zhang, Y. and Z. Yan, "A high-power wireless charging system using LCL-N topology to achieve a compact and low-cost receiver," *IEEE Transactions on Power Electronics*, Vol. 35, No. 1, 131–137, May 2019.
27. Ren, Y., J. W. Zhu, et al., "Electromagnetic, mechanical and thermal performance analysis of the CFETR magnet system," *Nuclear Fusion*, Vol. 55, 093002, 2015.
28. Ren, Y, "Magnetic force calculation between misaligned coils for a superconducting magnet," *IEEE Transactions on Applied Superconductivity*, Vol. 20, No. 6, 2350–2353, 2010.
29. Ren, Y., F. T. Wang, et al., "Mechanical stability of superconducting magnet with epoxy-impregnated," *Journal of Superconductivity and Novel Magnetism*, Vol. 23, No. 8, 1589–1593, 2010.
30. Hsueh, Y. and S. Su, "Decomposed fuzzy systems and their application in direct adaptive fuzzy control," *IEEE Transactions on Cybernetics*, Vol. 44, No. 10, 1772–1783, Oct. 2014.
31. Wang, N. N. and M. J. Er, "Direct adaptive fuzzy tracking control of marine vehicles with fully unknown parametric dynamics and uncertainties," *IEEE Transactions on Control Systems Technology*, Vol. 24, No. 5, 1845–1852, Sept. 2016.